PHASE-SPACE DISTANCE BETWEEN STATIONARY STATES MODULATES PHENOTYPIC PLASTICITY IN BREAST CANCER

MAYARA D. A. CALDAS[1], ALEXANDRE A. B. LIMA[2], FRANCISCO LOPES[3]

ABSTRACT. Transitions between stable states are a defining feature of nonlinear dynamical systems, yet the factors controlling their probabilities and timescales remain poorly understood in non-conservative settings. In many theoretical frameworks, such control is commonly interpreted in terms of potential depth, a concept that becomes ambiguous outside equilibrium. By analyzing a gene regulatory network associated with breast cancer subtypes, we uncover a geometric framework in which the phase-space distance between stationary states, together with the bifurcation structure organizing multistability, provides a robust and well-defined determinant of transition probabilities, times, and variability. Our results show that the coexistence of stable states is only a necessary condition for transitions, while their accessibility is constrained by geometric features of the underlying state space. Within this framework, we find that the HER2+ regime exhibits dynamical robustness to intrinsic parameter variations, whereas the TNBC regime displays strong sensitivity and amplified variability. These differences emerge naturally from the geometric organization of the bistable region and offer a dynamical explanation for the pronounced heterogeneity observed in TNBC. Together, our results establish a general geometric perspective on transitions in non-conservative regulatory networks, with implications for understanding phenotypic plasticity in complex biological systems.

1. INTRODUCTION

Breast cancer is the most commonly diagnosed cancer worldwide, with over 2.3 million new cases in 2022, and it is a leading cause of cancer-related deaths among women globally [1]. This disease is highly heterogeneous, both between patients and within individual tumors, which contributes to differences in prognosis, therapeutic response and clinical outcomes [2]. Clinically, breast tumors are often assigned intrinsic-like subtypes using immunohistochemical (IHC) surrogates for key hormone and growth factor receptors: estrogen receptor (ER), progesterone receptor (PR) and human epidermal growth factor receptor 2 (HER2), along with the proliferation marker Ki-67. In contrast, true molecular classification relies on multigene assays (e.g., [3]).

In clinical practice, four main subtypes are distinguished through these IHC markers. The so-called hormone receptor-positive tumors, Luminal A and B, show high levels of hormone receptors (estrogen (ER) and/or progesterone (PR)), with Luminal B being typically more aggressive. The two other subtypes are HER2-enriched (HER2+) and triple-negative breast cancer (TNBC). The first shows an overexpression of the HER2 receptor on the cell membrane, while TNBC does not exhibit significant levels of ER, PR, or HER2, which justifies its nomenclature [4]. Among these subtypes, triple-negative breast cancer (TNBC) stands out for its marked genetic and clinical variability, which correlates with its high aggressiveness and poor prognosis. This substantial variability has motivated numerous proposals for TNBC subclassification in the literature, underscoring the need for dynamical models that can capture its inherent plasticity and unpredictable behavior [5, 6].

Nuclear factor kappa B ($NF\text{-}\kappa B$) is a family of transcription factors composed of five members: RelA ($p65$), c-Rel, RelB, $NF\text{-}\kappa B1$ ($p50$), and $NF\text{-}\kappa B2$ ($p52$), expressed in nearly all cell types. These factors can form various homo- and heterodimer combinations, with the $p50/p65$ heterodimer being the most common and functionally relevant. Under basal conditions, $NF\text{-}\kappa B$ remains inactive in the cytoplasm bound to inhibitory $I\kappa B$ proteins; upon inflammatory stimuli, cellular stress, or growth signals, it is released and translocates to the nucleus, where it activates genes involved in inflammation, cell survival, proliferation and apoptosis resistance. Although $NF\text{-}\kappa B$ plays essential physiological roles, such as in mammary gland morphogenesis, its constitutive activation, particularly of the $p50$ and $p65$ subunits, is widely associated with breast cancer development and progression. Its activity contributes to remodeling the tumor microenvironment, promotes angiogenesis, epithelial-to-mesenchymal transition (EMT), stem-like features, and resistance to endocrine, chemotherapy, and radiotherapy treatments. In particular, elevated $NF\text{-}\kappa B$ levels are associated with aggressive tumors, favoring metastasis, early recurrence and reduced overall survival, highlighting $NF\text{-}\kappa B$ as a promising therapeutic target (see [7], [8]). This dual role underscores

[1,2,3] DEVELOPMENTAL BIOLOGY AND DYNAMICAL SYSTEMS GROUP, UNIVERSIDADE FEDERAL DO RIO DE JANEIRO, CAMPUS DUQUE DE CAXIAS PROFESSOR GERALDO CIDADE; DUQUE DE CAXIAS, BRAZIL.

E-mail address: [1] mayaraduartecaldas@gmail.com, [2] assis@caxias.ufrj.br, [3] flopes@ufrj.br.

Key words and phrases. breast cancer; bifurcation diagrams; $NF\text{-}\kappa B$.

the need to dissect its cancer-specific activation pathways to develop targeted interventions that can inhibit its pro-tumorigenic functions while sparing its essential physiological activities, thereby minimizing adverse effects.

While breast cancer subtypes are clinically treated as distinct entities with subtype-specific therapies, recent single-cell RNA sequencing (scRNA-seq) studies ([9], [10]), which measure the relative expression levels of all genes across hundreds of individual cells, challenge this notion. These experiments have revealed substantial intra-tumoral heterogeneity, including the presence of cells classified as belonging to other subtypes (e.g., TNBC cells within clinically classified HER2+ tumors). This heterogeneity plays a critical role in treatment resistance due to the targeted nature of contemporary therapies, underscoring the urgent need to understand the underlying dynamical mechanisms in order to develop strategies that can overcome resistance and reduce the societal burden of the disease.

The cancer attractors paradigm conceptualizes phenotypic states as attractor basins in an epigenetic landscape ([11], [12], [13]), with transitions governed by the crossing of potential barriers. While influential, this framework relies on the metaphor of an energy landscape, which assumes a conservative system, an assumption that breaks down for real gene regulatory networks characterized by continuous synthesis and degradation (source and sink terms). Since actual biological networks are non-conservative, the barrier height between attractors lacks both a theoretical definition and experimental measurability.

Given the critical role of $NF\text{-}\kappa B$ in breast cancer aggressiveness, treatment resistance and the complexity of its intracellular interactions, mathematical modeling offers a powerful approach to investigate its underlying regulatory mechanisms. Based on precise experimental data and well documented gene regulatory interactions ([14], [15], [16]) we have previously developed a gene regulatory network (GRN) describing $NF\text{-}\kappa B$ role in its own regulation and some key genes involved in EMT, such as TWIST1, SNAIL, and SIP1 ([17]). The model bistable dynamics give rise to two stable fixed points, corresponding to the characteristic gene expression profiles of the HER2+ and TNBC subtypes. These attractors are separated by an unstable steady state and are each surrounded by their own basin of attraction. Critically, the model provides a mechanistic explanation for observed intra-tumoral heterogeneity: stochastic fluctuations in gene expression can drive spontaneous, irreversible transitions from the HER2+ to the TNBC attractor at randomly distributed times.

To systematically understand how key regulatory interactions control this phenotypic plasticity, we present here a comprehensive bifurcation analysis. We focus on a simplified sub-model containing only the core $NF\text{-}\kappa B$ self-regulatory mechanism, as its intrinsic positive feedback is the primary driver of the bistability and state transitions. This simplification allows us to capture the essential dynamics without the additional complexity of EMT-related $NF\text{-}\kappa B$ target genes.

We first performed single-parameter bifurcation analyses to characterize the bistable regions and assess the model sensitivity to different variables. To connect these deterministic landscapes to cellular behavior, we performed stochastic simulations to evaluate how the distance between stationary points affects transition probabilities. Finally, we performed two-parameter bifurcation analysis to understand how combined parameter changes affect the system's dynamic behavior.

Our analysis reveals that the TNBC state is highly susceptible to natural variations in kinetic parameters, as may occur between patients or even among cells within the same tumor. At a more fundamental level, however, the results reported here provide a conceptual advance to the cancer attractors paradigm by identifying a geometric control mechanism for phenotypic transitions.

Specifically, we show that transition probabilities are governed by the phase-space distance between stable and unstable stationary states of the regulatory network. Unlike the abstract notion of potential barrier height, this distance is a well-defined quantity in non-conservative systems and can be directly computed from the kinetic parameters of the network, which are, in principle, experimentally measurable (e.g., degradation rates or binding affinities). In this way, our approach replaces an inaccessible metaphor with a quantitative, network-derived predictor of phenotypic plasticity.

2. Results

2.1. **Breast cancer subtypes map onto two basins of attraction.** We study a gene regulatory network model describing the self-regulation of $NF\text{-}\kappa B$, originally introduced in [17]. The model focuses on the role of the transcription factor $NF\text{-}\kappa B$ in driving breast cancer heterogeneity. Specifically, it describes the regulation of the $p50$ and $p65$ genes by $NF\text{-}\kappa B$, which in turn encode the synthesis of the $p50$ and $p65$ subunits of $NF\text{-}\kappa B$ itself. By capturing this positive feedback loop, the model incorporates two mechanisms that have been shown to play critical roles in gene regulation and development: positive feedback [18] and dimer formation [19]. This framework allows us to investigate how $NF\text{-}\kappa B$ dynamics contribute to cancer cell progression and phenotypic heterogeneity.

Figure 1 depicts the gene regulatory network. Its components and reactions are described below:

- $N0X$: Denotes the unbound (unoccupied) regulatory region of gene X.
- $N1X$: Denotes the region of gene X bound by an $NF\text{-}\kappa B$ dimer.
- Gene X: $p50$ or $p65$.

Gene activation is described by a three-step process:

- Reversible binding of $NF\text{-}\kappa B$ to the gene's regulatory region: $NF\text{-}\kappa B + N0X \leftrightarrow N1X$.
- Irreversible RNA synthesis: $N1X \rightarrow N1X + RNAX$.
- Irreversible protein synthesis: $RNAX \rightarrow RNAX + X$.

In addition, the model describes the following constitutive reactions:

- Constitutive RNA synthesis: $0 \rightarrow RNAX$.
- RNA degradation: $RNAX \rightarrow 0$.
- Protein degradation: $X \rightarrow 0$.
- Dimer formation: $NF\text{-}\kappa B \leftrightarrow p50 + p65$.

These sequential reactions describe the transcription factor $NF\text{-}\kappa B$ binding to the promoter region of the $p65$ gene, promoting its transcriptional activation. Once activated, the gene is transcribed into messenger RNA, which is subsequently translated into the $p65$ protein. A similar process occurs with the $p50$ gene: $NF\text{-}\kappa B$ binds to its promoter, inducing the production of $RNAp50$ and consequently the corresponding $p50$ protein. These two proteins, $p50$ and $p65$, associate in the cytoplasm to form new $NF\text{-}\kappa B$ dimers. This establishes a positive feedback loop in which $NF\text{-}\kappa B$ activates the expression of the very genes that encode its own subunits, thereby reinforcing its activity and enabling sustained regulatory dynamics.

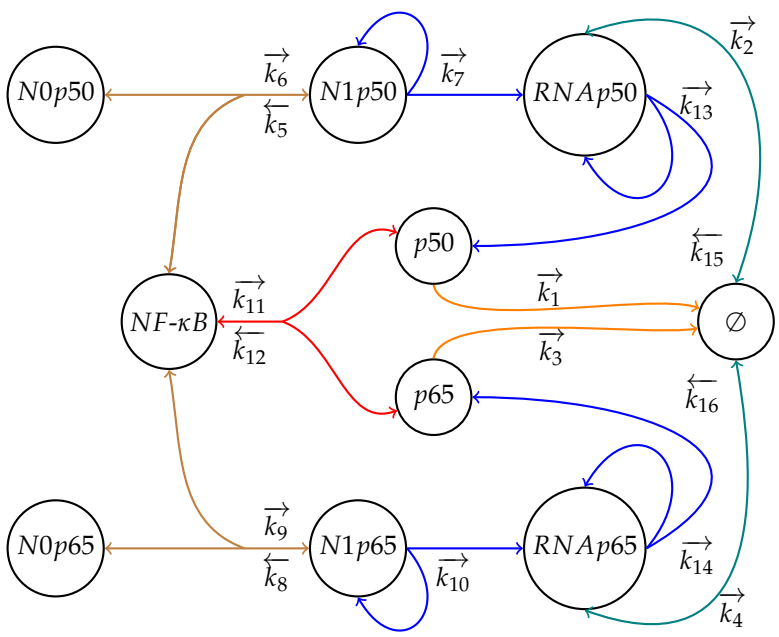

FIGURE 1. $NF\text{-}\kappa B$ Gene Regulatory Network. Brown lines represent $NF\text{-}\kappa B$ binding to the $p50/p65$ gene promoter. Red represents dimerization. Blue indicates RNA and protein synthesis. Orange represents degradation. Teal indicates constitutive synthesis and degradation. The kinetic constant $\overrightarrow{k_i}$ and $\overleftarrow{k_j}$ are associated to the forward and reverse reactions respectively. See Table S1 for traditional representation.

By applying the law of mass action ([20]) to the reactions described in the regulatory network (Figure 1) we obtain the following system of ordinary differential equations:

$$
(1)\quad \begin{cases}
\dfrac{dRNAp50}{dt} &= k_{15} - k_2 RNAp50 + k_7(-N0p50 + NTp50),\\[2ex]
\dfrac{dRNAp65}{dt} &= -k_4 RNAp65 + k_{10}(-N0p65 + NTp65) + k_{16},\\[2ex]
\dfrac{dNF\text{-}\kappa B}{dt} &= k_5(-N0p50 + NTp50) - k_6 NF\text{-}\kappa BN0p50 + k_8(-N0p65 + NTp65) - k_9 NF\text{-}\kappa BN0p65 - k_{11} NF\text{-}\kappa B + k_{12} p50p65,\\[2ex]
\dfrac{dN0p50}{dt} &= k_5(-N0p50 + NTp50) - k_6 NF\text{-}\kappa BN0p50,\\[2ex]
\dfrac{dN0p65}{dt} &= k_8(-N0p65 + NTp65) - k_9 NF\text{-}\kappa BN0p65,\\[2ex]
\dfrac{dp50}{dt} &= -k_1 p50 + k_{11} NF\text{-}\kappa B - k_{12} p50p65 + k_{13} RNAp50,\\[2ex]
\dfrac{dp65}{dt} &= -k_3 p65 + k_{11} NF\text{-}\kappa B - k_{12} p50p65 + k_{14} RNAp65.
\end{cases}
$$

From [17], we used

$$
(2)\quad \begin{gathered}
k_1 = 0.03013253683,\ k_2 = 0.1015001600,\ k_3 = 0.05250597525,\ k_4 = 0.1078479760,\ k_5 = 82909.01811,\\
k_6 = 0.9028654817,\ k_7 = 37.06962815,\ k_8 = 104.8833566,\ k_9 = 0.0008908866630,\ k_{10} = 56.23070180,\\
k_{11} = 1.696832619,\ k_{12} = 0.000002663192070,\ k_{13} = 9.379999999,\ k_{14} = 44.95000000,\\
k_{15} = 6.123047904,\ k_{16} = 9.197393172,\ NTp50 = 2 \ \text{ and } \ NTp65 = 2.
\end{gathered}
$$

All kinetic parameters are treated as dimensionless in the main text for simplicity, with their corresponding dimensional forms and units reported in Table S1. The model admits three stationary points. A linear stability analysis shows that two are locally asymptotically stable, with all eigenvalues having negative real parts, and one is unstable, with one eigenvalue having a positive real part. This configuration characterizes the system as bistable, since it possesses two stable steady states separated by an unstable one. The parameters in (2) were determined using experimental data on the RNA levels of $NF\text{-}\kappa B$ in two well-known cell lines, HCC-1954 and MDA-MB-231, classified as subtypes HER2+ and triple negative breast cancer (TNBC), respectively. A key characteristic of these cells is the high level of $NF\text{-}\kappa B$ in the TNBC subtype compared to HER2+. The model bistable behavior was key for the model calibration because it allowed for the same set of parameter to reproduce both stable levels of $NF\text{-}\kappa B$ identified in each BC subtype cell lines. Both stable states are represented in Figure 2, together with the unstable one. Below, we present the stationary points, listing the copy number of $RNAp50$, $RNAp65$, $NF\text{-}\kappa B$, $N0p50$, $N0p65$, $p50$, and $p65$, respectively:

$$
\begin{gathered}
\text{HER2+} = (104.376, 134.992, 5893.33, 1.87939, 1.90466, 32491.3, 115566),\\
\text{Unstable} = (245.66, 303.86, 31221.9, 1.49254, 1.58078, 76472, 260132),\\
\text{TNBC} = (483.441, 625.248, 126429, 0.84147, 0.964367, 150491, 535271).
\end{gathered}
$$

The ability of our bistable model to reproduce $NF\text{-}\kappa B$ expression profiles of two breast cancer subtypes provides evidence for the cancer attractor framework, in which cellular phenotypes correspond to stable attractor states shaped by gene regulatory dynamics.

Considering the calibrated model, we computed the Euclidean distance between the stationary states in the phase space, where each axis corresponds to the absolute molecule count of a species. This distance, reported in molecule copy number (c.n.), quantifies the aggregate change in molecular abundance required to traverse between states. The distance between the HER2+ state and the unstable point is 153216.35 m.u., while for the TNBC state it is 300407.21 m.u., indicating that the unstable point is much closer to the HER2+ state, almost half the distance compared to TNBC. Notably, stochastic single-cell simulations by Lopes *et al*. [17] demonstrated that HER2+ tumors can evolve into the TNBC subtype, with 120 simulated trajectories showing this transition over a 20-year period.

These findings raise an important question: how can parameter variation increase these distances and potentially prevent transitions between subtypes?

To address this, in the next section we show bifurcation analyses with respect to each system parameter, enabling us to evaluate how the distances between the stationary states depend on parameter values.

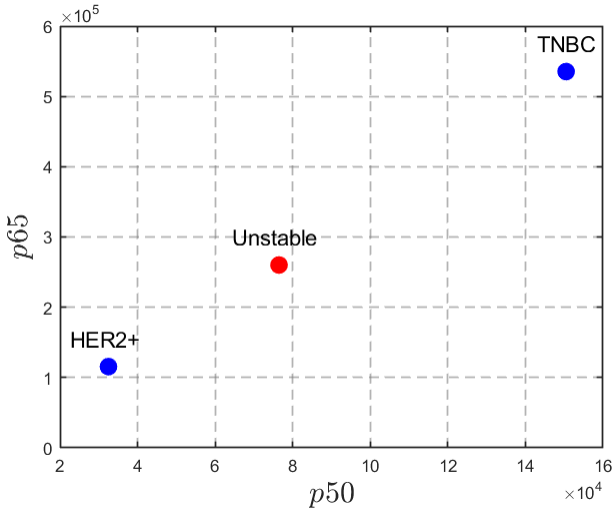

FIGURE 2. Projection of the system's stationary states onto the $p50 \times p65$ plane, highlighting the coexistence of two stable phenotypic states (HER2+ and TNBC) separated by an unstable saddle point. Expression levels are shown as absolute numbers of molecule copies.

2.2. **Bifurcation analysis shows that TNBC is highly sensitive to parameter variation.** Our bifurcation analysis aimed to map how the parameter space governs phenotypic stability. To this end, we first characterized how variations in key parameters modulate the concentrations of species within each basin of attraction, thereby assessing the sensitivity of each attractor to perturbations. This analysis was performed using the numerical continuation software MATCONT ([21]), a numerical tool widely used for characterizing bifurcations in systems of ordinary differential equations. Initially, we examined the effect of varying the parameter k_3, which corresponds to the degradation reaction $p65 \to 0$, and its influence on the dynamics of $NF\text{-}\kappa B$.

The continuation analysis reveals that saddle-node bifurcations control the phenotypic transition between HER2+ and TNBC breast cancer subtypes, with the parameter k_3 playing a critical role in this process by modulating $NF\text{-}\kappa B$ expression levels. Figure 3 displays the $NF\text{-}\kappa B$ bifurcation diagram with respect to k_3, highlighting regions of monostability and bistability. This diagram exhibits the inverted S-shaped curve, characterized by two saddle-node bifurcations that delimit three distinct regions of the parameter k_3:

- For $k_3 \in (0.0403, 0.048)$, the system has a monostable region, associated with the TNBC phenotype.
- For $k_3 \in (0.048, 0.056)$, the system exhibits bistability, characterized by the coexistence of two stable solutions (HER2+ and TNBC states) separated by an unstable point.
- For $k_3 \in (0.056, 0.0655)$, the system exhibits only a monostable region, in this case associated with the HER2+ phenotype.

The geometry of the bifurcation curve reflects different sensitivities associated with the TNBC and HER2+ phenotypes. Its lower branch, corresponding to the HER2+ phenotype, is characterized by low levels of $NF\text{-}\kappa B$ and by a relatively small variation in its concentration across a wide range of k_3 values. This behavior indicates that, in this regime, the system is only weakly sensitive to changes in the degradation rate of $p65$. As a result, small variations in k_3 are not sufficient to significantly perturb the $NF\text{-}\kappa B$ levels. In contrast, the upper branch, associated with the TNBC phenotype, exhibits a steeper slope, reflecting a much higher sensitivity to changes in k_3. Thus, variation in k_3, which changes the degradation rate of $p65$, leads to a marked variation in the stationary level of $NF\text{-}\kappa B$.

Figure 4 shows the bifurcation diagrams for all remaining variables with respect to k_3. The variables $RNAp50$, $RNAp65$, $p50$ and $p65$ all exhibit the same inverted S-shaped curve as $NF\text{-}\kappa B$. This trend occurs because k_3 sets the degradation rate of $p65$: higher values of k_3 lead to lower steady-state levels of these variables, which is characteristic of the HER2+ subtype. In contrast, the diagrams for $N0p50$ and $N0p65$ display the opposite pattern, that is, an S-shaped curve. This behavior occurs because $N0p50$ and $N0p65$ represent unoccupied gene regulatory regions; therefore, a greater k_3 value leads to a lower amount of $NF\text{-}\kappa B$, making more of these regions available (i.e., unbound).

To determine how the system's variables are affected by the parameter k_3 along the different bifurcation branches, we performed a sensitivity analysis. The results are summarized in Table 1. We also show the percentage variation

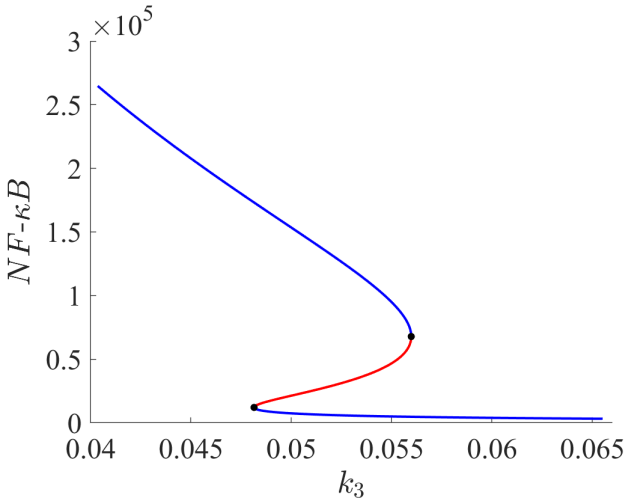

FIGURE 3. Bifurcation diagram of $NF\text{-}\kappa B$ with respect to k_3. Stable solutions are represented in blue, while unstable solutions are represented in red.

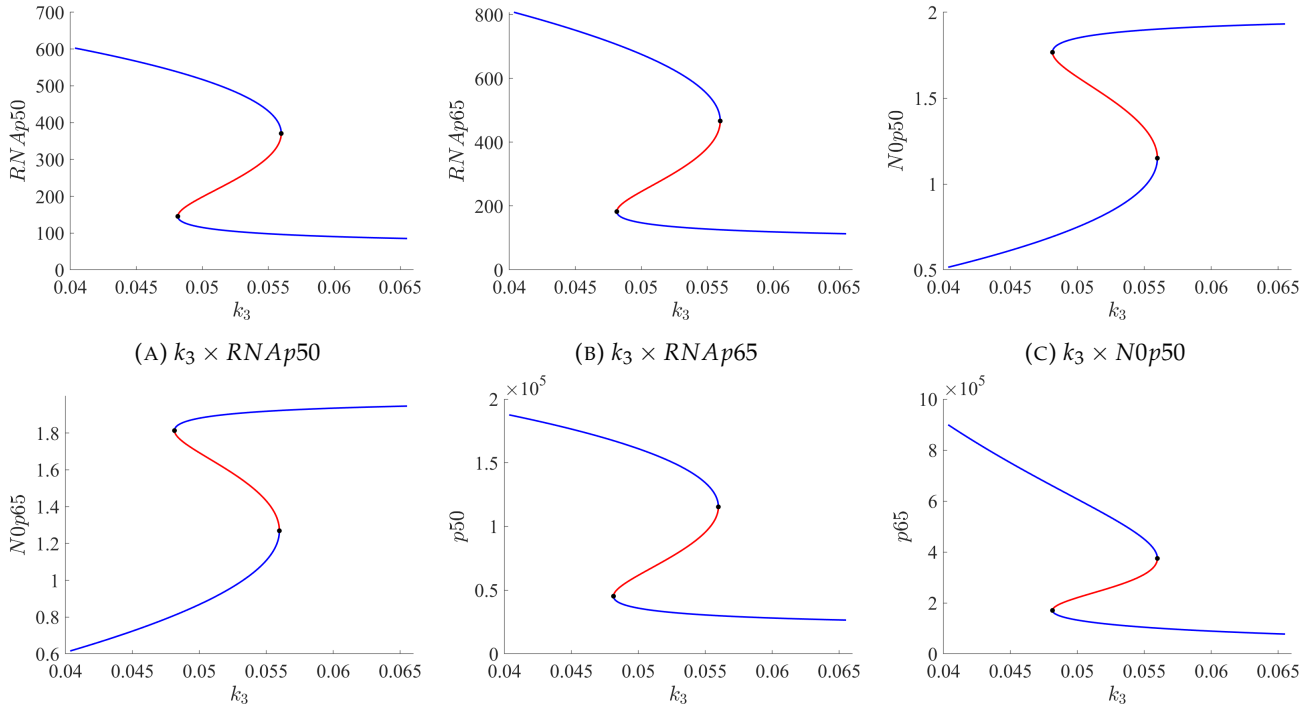

(A) $k_3 \times RNAp50$ (B) $k_3 \times RNAp65$ (C) $k_3 \times N0p50$

(D) $k_3 \times N0p65$ (E) $k_3 \times p50$ (F) $k_3 \times p65$

FIGURE 4. Bifurcation diagrams of all species, except $NF\text{-}\kappa B$, with respect to k_3. Stable solutions are represented in blue, while unstable solutions are represented in red.

for each branch relative to the total variation (set to 100%). Figure 5 shows the relative sensitivity of each variable to k_3, indicating that, in the TNBC branch, all variables are highly sensitive to this parameter.

Interestingly, although $p65$ would be expected to be more sensitive to k_3 since this parameter is related to its degradation rate, $NF\text{-}\kappa B$ instead shows higher sensitivity in the TNBC branch. This unexpected behavior stems from the combined effect of dimerization to form $NF\text{-}\kappa B$ and its role in $p50$ and $p65$ synthesis. A reduction in $p65$ causes a reduction in the levels of $NF\text{-}\kappa B$ dimers, which results in lower levels of $p50$ and $p65$. Consequently, with fewer monomers available, the level of $NF\text{-}\kappa B$ is doubly affected. This high sensitivity may be linked to a clinical

characteristic of TNBC: its significant variability among breast cancer subtypes. Consequently, several new TNBC subclassifications have recently been proposed. We explore this potential connection further in the Discussion.

In contrast to the sensitivity pattern in the TNBC branch, the concentration of all species in the lower branch, associated with HER2+, exhibits remarkably lower sensitivity to k_3 (compare the percentage variation for each variable, Table 1). This indicates that gene expression levels in this subtype are more stable than in TNBC. This difference is even more pronounced for $NF\text{-}\kappa B$ concentration: the TNBC branch exhibits a 75.29% variation, compared to only 3.39% for the HER2+ branch. This suggests that, in the low protein level regime, the combined effects of dimerization and $NF\text{-}\kappa B$ play no significant role. This has a strong downstream effect, indicating that the expression levels of $NF\text{-}\kappa B$ target genes are expected to show lower sensitivity to k_3, even when compared to the sensitivity of $p50$ and $p65$ levels.

Variables	**TNBC**	**HER2+**	**Total**	**% TNBC**	**% HER2+**
$RNAp50$	231.99	60.27	517.52	44.83	11.65
$RNAp65$	340.60	69.40	693.96	49.08	10.00
$NF\text{-}\kappa B$	196895.13	8877.67	261499.54	75.29	3.39
$N0p50$	0.64	0.16	1.42	44.83	11.65
$N0p65$	0.65	0.13	1.33	49.08	10.00
$p50$	72216.78	18762.52	161098.68	44.83	11.65
$p65$	524527.20	92805.19	821504.67	63.85	11.30

TABLE 1. Variation of each species' copy number along the HER2+ and TNBC branches as a function of k_3 in the corresponding bifurcation diagrams. The columns are as follows: (1) variables; (2) absolute variation along the TNBC branch; (3) absolute variation along the HER2+ branch; (4) total absolute variation across the entire bifurcation diagram; (5-6) the percentage values, with column (4) representing 100%.

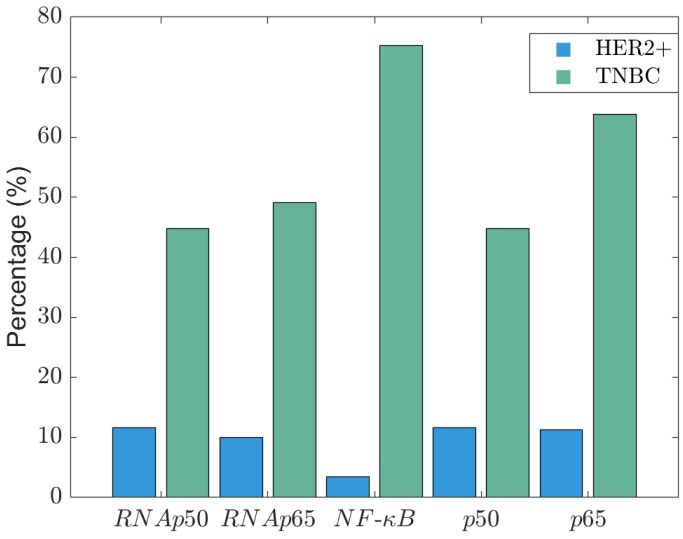

FIGURE 5. Sensitivity of each species to parameter k_3. Blue and green bars represent the sensitivity based on the total percentage variation in the HER2+ and TNBC subtype branches, respectively.

The analysis performed for the parameter k_3 can be extended to the remaining parameters in the GRN, Figure 1. The bistable and monostable intervals of all parameters are provided in Table S2, within the "Bifurcation diagrams

with a free parameter" section of the Supplementary Material. The intervals of values for all variables on both stable branches, along with the respective bifurcation diagrams for each model parameter, are also presented (Tables $S3$, $S4$ and $S(n+1)$ and Figures $S1$, $S2$ and $S(n-1)$ for k_1, k_2, and k_n, $n = 4, ..., 16$, respectively). The sensitivity analyses are shown in Figure S16. Selected cases from these results are discussed below.

All NF-κB bifurcation diagrams with respect to the kinetic parameter associated with the forward self-activation reactions, together with constitutive RNA synthesis, exhibit an S-shaped curve (see Figures Si, i = 5, 6, 8, 9, 11, 12, 13, 14, 15). This is expected since all these reactions lead to increasing NF-κB levels. Consequently, the higher these parameters are, the higher the NF-κB levels will be, leading the upper side of the S-shaped curve to the right side. Conversely, the bifurcation diagram with respect to the kinetic parameter associate to all reactions contributing to reducing NF-κB levels show inverted S-shaped curves (Figure 3 and Figures Si, $i = 1, 2, 3, 4, 7, 10$). Interestingly, while the reactions $N1p50 \rightarrow N0p50 + NF\text{-}\kappa B$ and $N1p65 \rightarrow N0p65 + NF\text{-}\kappa B$, associated with the kinetic parameters k_5 and k_8, respectively, initially appear to increase NF-κB levels, they ultimately reduce them because these reactions decrease the levels of $N1p50$ and $N1p65$. This leads to reduced synthesis of $p50$ and $p65$ and, consequently, lower NF-κB levels. Besides that, since the maximum amount of $N1p65$ and $N1p50$ is 2 (corresponding to both gene copies being bound), the contribution of these reactions towards increasing NF-κB is insignificant. In all cases, the upper branch corresponds to the TNBC subtype, whereas the lower branch corresponds to the HER2+ subtype. Moreover, in all the NF-κB diagrams, the lower branch is consistently less sensitive to parameter variations, whereas the upper branch shows greater responsiveness.

Figure S16 shows the sensitivity analysis for the bifurcation diagram of all species with respect to all parameters, except k_3. It reveals that in the TNBC branch, NF-κB is the most sensitive variable to parameter variations across all diagrams. Conversely, in the HER2+ branch, it is the least sensitive variable in all diagrams. This indicates that in the HER2+ subtype branch, the variability of all variables is buffered at the level of NF-κB, while in the TNBC subtype branch, it is amplified. This pattern mirrors the one observed in the bifurcation diagrams with respect to k_3 (Figure 5) and likely contributes to the high clinical variability found in TNBC-classified tumors.

2.3. **The distance between phenotypic states modulates transition times.** The arrangement between the stationary states, Subsection 2.1, reveal an important geometric feature: the unstable saddle point lies much closer to the HER2+ attractor than to the TNBC attractor, indicating an asymmetric separation between the two phenotypic basins. This observation raises the question of whether parameter variations could modify these distances and thereby prevent transitions between subtypes. To investigate this, we focused on parameters k_3 and k_{12}, which correspond to the reactions $p65 \rightarrow 0$ and $p50 + p65 \rightarrow NF\kappa B$, respectively. These reactions have the strongest impact on $NF\kappa B$ levels. Since the analysis centers on distances between stationary points, it is restricted to the bistable region for each parameter. For various parameter values within the bistable region, we calculated the distances between the HER2+ and unstable point, as well as between the TNBC and unstable point. These distances were subsequently interpolated to produce continuous curves, Figure 6.

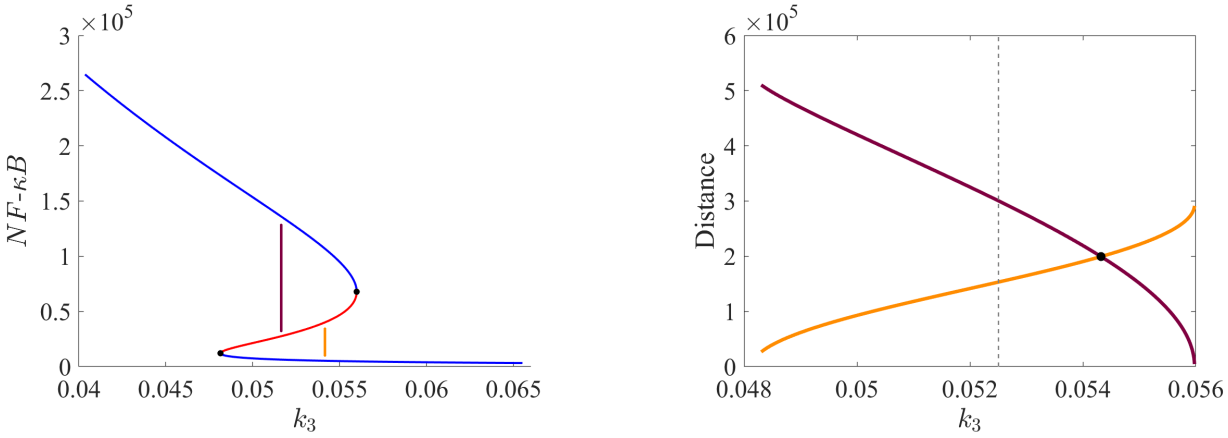

(A) $k_3 \times NF$-κB (B) Distance

FIGURE 6. Variation of distances between stationary points with respect to k_3. Brown and orange lines denote the distance from TNBC to the unstable point and from the unstable point to HER2+, respectively. (A) Bifurcation diagram of k_3, indicating the distance between stationary states. (B) Variation of these distances, reported in c.n., as a function of k_3, with the dashed line corresponding to the value of k_3 in the original system. ($k_3 = 0.05250597525$).

Figure 6a shows the $NF\kappa B$ bifurcation diagram with respect to k_3 indicating how the distance between states were determined. From the left border of the bistable region toward higher k_3 values, the distance between the HER2+ and the unstable state increases gradually (Figure 6b, orange curve), while the distance between the unstable and the TNBC state decreases, brown curve. Both distances become identical (199405.21 c.n.) at $k_3 = 0.054321555749$, with a relative error of only 8.099×10^{-10} (i.e., 8.10×10^{-8}%). This k_3 value corresponds to a 3.46% increase compared to the originally calibrated value ($k_3 = 0.05250597525$), Table 2. Such an increase in k_3 results in a 30.15% increase in the distance between HER2+ and the unstable state, and a 33.62% decrease in the distance between the unstable and TNBC states.

To further explore the role of this kinetic parameter for the transition between states, we tested the effect of a 19.94% reduction in the distance from HER2+ to the unstable state, from the original 153216.35 c.n. to 122670.94 c.n.. This was achieved by a 2.5% decrease in k_3 from the originally value. The distance from the unstable state to TNBC was increased by 21.18%.

Table 2 summarizes all distances from HER2+ and TNBC to the unstable state for three different k_3 values considered, together with their percentage variations relative to the original calibrated value.

k_3	Variation (%)	HER2+ $\leftrightarrow$ Unstable	Variation (%)	TNBC $\leftrightarrow$ Unstable	Variation (%)
0.05250597525	Not apply	153216.35	Not apply	300407.21	Not apply
0.054321555749	$\uparrow$ 3.46%	199405.21	$\uparrow$ 30.15%	199405.21	$\downarrow$ 33.62%
0.0511933259	$\downarrow$ 2.5%	122670.94	$\downarrow$ 19.94%	364024.90	$\uparrow$ 21.18%

TABLE 2. Distances, in c.n., from HER2+ and TNBC to the unstable state for different k_3 values, and their percentage variations relative to the original.

To assess the impact of these altered distances between stable states on subtype transitions, we performed 120 stochastic simulations using COPASI (see [22]). For the values of k_3 that placed the unstable state at the midpoint between HER2+ and TNBC, none of the 120 simulations exhibited a transition from HER2+ to TNBC, even after 20 years of simulated time. A randomly selected simulation (Figure 7) shows the system fluctuating around the HER2+ stable state. This behavior was expected, since for this k_3 value the distance from HER2+ to the unstable point is increased by 30.15% compared to the original calibration.

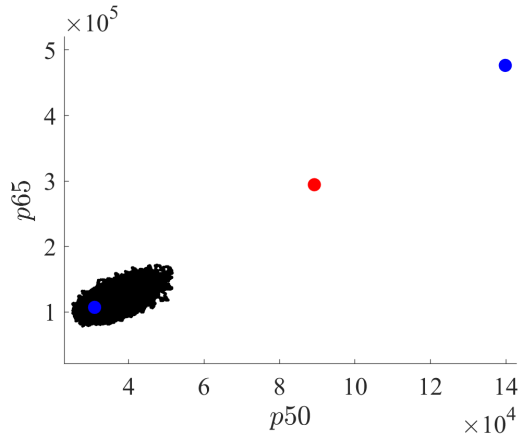

FIGURE 7. Stochastic model simulation for $k_3 = 0.054321555749$, which places the unstable state at the midpoint between HER2+ and TNBC states. Over a time period of 20 years, the model remains fluctuating around HER2+.

For $k_3 = 0.0511933259$ (a 2.5% reduction from the original value), which shortens the HER2+–unstable distance by 19.94%, all 120 simulations transitioned from HER2+ to TNBC within 18 days (Figure 8a). The trajectory in Figure 8b illustrates this rapid transition: the system spends only a brief time fluctuating around the HER2+ state before moving to the TNBC basin.

In addition to k_3, analyzed above, the dimer association parameter k_{12} is also critical for NF-κB levels (Figure 9a). However, unlike k_3, for higher values of k_{12} the system settles into the TNBC attractor, exhibiting NF-κB

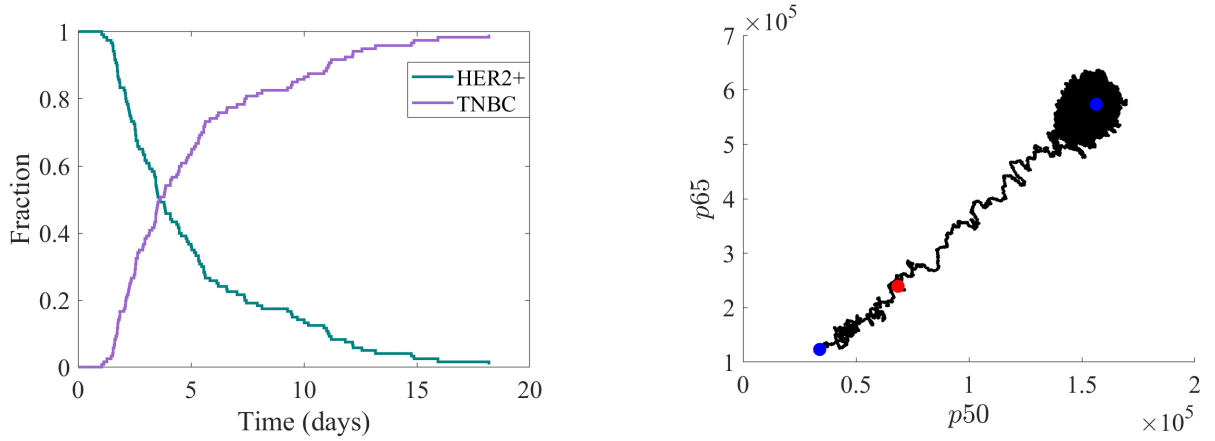

(A) Fraction of cells in each subtype.

(B) Trajectory in the p50 versus p65 phase space.

FIGURE 8. Stochastic simulations for $k_3 = 0.0511933259$. (A) Fraction of HER2+ and TNBC cells over time across 120 simulations. All simulations start as HER2+ (fraction = 1) and complete the transition to TNBC (fraction = 1) within 18 days. (B) Transition trajectory from HER2+ to TNBC in the $p50$ versus $p65$ phase space.

levels characteristic of the TNBC subtype. Moving inside the bistable region from left to right increases the distance between TNBC and the unstable state (brown curve in Figure 9b). In this case, the value of k_{12} for which the unstable state is equidistant from HER2+ and TNBC is $k_{12} = 2.574339 \times 10^{-6}$, with a relative error of 4.5968×10^{-6} (i.e., 0.0004596814%), and the corresponding distance is 199405.21 c.n.. To verify the transition probabilities under these conditions, we performed 120 stochastic simulations with this value of k_{12}. Over 20 years of simulated time, no transitions to the TNBC state were observed in any simulation, confirming the high stability of the HER2+ state. This behavior mirrors the stability observed when varying k_3. As shown in the representative trajectory (Figure 10), the system fluctuates around the HER2+ steady state, reflecting the increased distance between it and the unstable state compared to the original configuration.

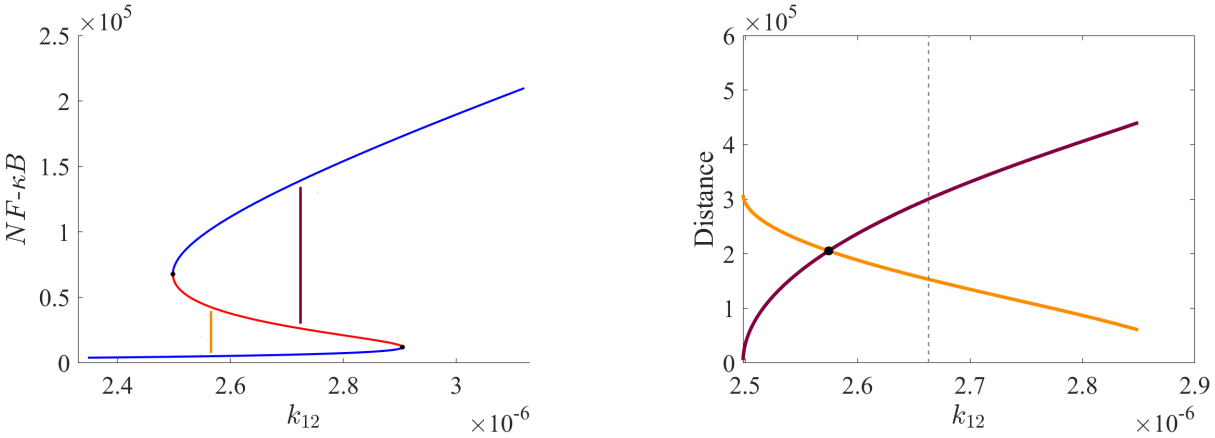

(A) $k_{12} \times NF\text{-}\kappa B$

(B) Distance

FIGURE 9. Distance with respect to k_{12}. Brown and orange lines denote the distance from TNBC to the unstable point and from the unstable point to HER2+, respectively. (A) Bifurcation diagram of k_{12}, indicating the distance between stationary states. (B) Variation of these distances, reported in c.n., as a function of k_{12}, with the dashed line corresponding to the value of k_{12} in the original system. ($2.66319207 \times 10^{-6}$).

It is remarkable how quickly the transition from HER2+ to TNBC occurs when the original HER2+–unstable state distance is reduced to 122670.94 c.n. by decreasing k_3 by 2.5%; all 120 simulations transitioned in less than 18 days (Figure 8a). To investigate whether this behavior is preserved when the same distance is achieved by

varying a different kinetic parameter, we increased the value of k_{12} by 2.35% such that the HER2+-unstable distance matched the same distance (122670.94 c.n.), Table 3. This reduced distance consistently facilitated rapid transitions, with all 120 simulations switching from HER2+ to TNBC within 32 days. As shown in the representative trajectory (Figure 11b), the system displayed only brief fluctuations around HER2+ state before transitioning to TNBC.

k_{12}	Variation (%)	HER2+ ↔ Unstable	Variation (%)	TNBC ↔ Unstable	Variation (%)
$2.663192070 \times 10^{-6}$	Not apply	153216.35	Not apply	300407.21	Not apply
2.574339×10^{-6}	↓ 3.33%	205386.83	↑ 34.05%	205385.89	↓ 31.63%
2.725683×10^{-6}	↑ 2.35%	122670.94	↓ 19.94%	351952.23	↑ 17.16%

TABLE 3. Distances, in c.n., from HER2+ and TNBC to the unstable state for different k_{12} values, and their percentage variations relative to the original.

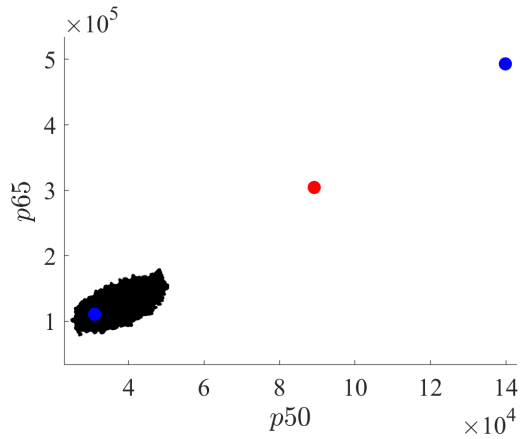

FIGURE 10. Representative stochastic simulation for the k_{12} value (2.574339×10^{-6}) at which both HER2+-unstable and unstable-TNBC distances are equal (205386.83 c.n.). The simulation illustrates the persistence of the HER2+ state over 20 years.

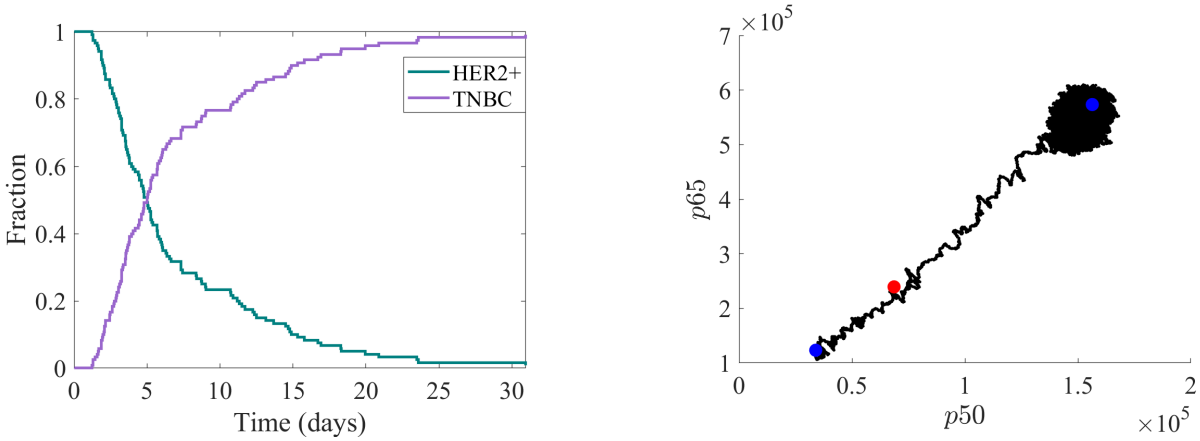

(A) Time course of HER2+ to TNBC transition.

(B) Phase-space trajectory of $p50$ versus $p65$.

FIGURE 11. Stochastic simulation for a reduced distance between the HER2+ and unstable states ($k_{12} = 2.725683 \times 10^{-6}$). (A) Fraction of HER2+ and TNBC cells over time. All simulations start as HER2+ (fraction = 1) and complete the transition to TNBC (fraction = 1) within 32 days. (B) Phase-space transition trajectory from a randomly selected simulation.

Our analysis above showed that setting the HER2+-unstable distance to 122670.94 c.n., either by choosing $k_3 = 0.054321555749$ or $k_{12} = 2.725683 \times 10^{-6}$, resulted in different transition times: 18 and 32 days, respectively. To deeper our analysis about these different behaviors according to the parameter changed, we fitted the distribution of the time of transition from each set of 120 simulations to log-normal probability density functions, as shown in Figure 12. The resulting statistical measures are summarized in Table 4.

Parameter	Mode (days)	Median (days)	Mean (days)	Variance (days^2)
k_3	2.416	3.885	4.928	14.772
k_{12}	2.927	5.115	6.761	34.164

TABLE 4. Statistical measures of transition times from 120 stochastic simulations for k_3 and k_{12}, both yielding the same HER2+-unstable state distance (122670.94 c.n.).

The most probable transition time (mode) for $k_3 = 0.054321555749$ is shorter than that for $k_{12} = 2.725683 \times 10^{-6}$, consistent with the full transition times (18 versus 32 days, respectively).

It is interesting to note that, to reach the 122,670.94 c.n. distance between the HER2+ and the unstable state, k_{12}, associated with the reaction $p50 + p65 \rightarrow NF\kappa B$, was increased by 2.35%, whereas k_3, associated with $p65 \rightarrow 0$, was reduced by 2.5%. Together with the statistics presented in Table 4, this indicates that the network is more sensitive to variations in the reaction $p50 + p65 \rightarrow NF\kappa B$ than in $p65$ degradation.

Notably, although variations in either parameter significantly accelerate transitions, changes in k_{12} lead to a broader distribution of transition times, reflecting increased variability in the system's dynamics. In other words, perturbations in the dimerization reaction have a stronger and more heterogeneous impact on the transition process than changes in $p65$ degradation.

Taken together, these findings indicate that while the distance between stationary states is a critical determinant of transition probabilities, it is not the sole factor governing the system's dynamics.

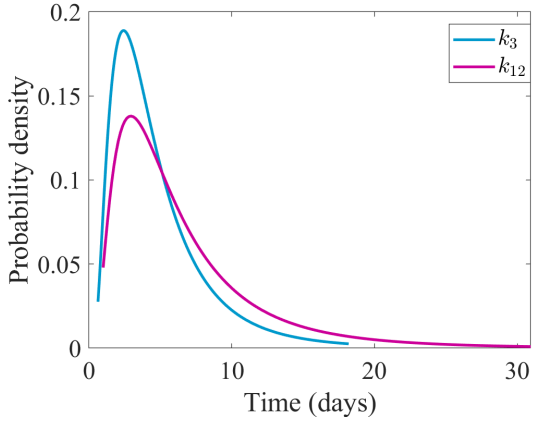

FIGURE 12. Log-normal distributions of transition times between the HER2+ and the unstable states, with the distance set to 122670.94 c.n.. Shown in teal-blue for k_3 reduced to 0.0511933259 and in dark magenta for k_{12} increased to 2.725683×10^{-6}.

2.4. **Parameter choice determines cusp geometry, resulting in unbounded or limited bistable regions.** Following the previous single-parameter analysis, we extended the study to the simultaneous variation of two model parameters. This analysis enables the identification of regions in parameter space corresponding to distinct dynamic regimes and the characterization of bifurcation curves and critical boundaries. Together, these results provide a more comprehensive understanding of how pairs of parameters jointly shape the system's global dynamics.

Since the levels of $NF\text{-}\kappa B$ and its subunits are critical for breast cancer progression, we first consider the simultaneous variation of parameters k_3 and k_{12}, which correspond to the degradation of $p65$ protein ($p65 \rightarrow 0$) and the dimerization ($p50 + p65 \rightarrow NF\text{-}\kappa B$), respectively. The MATCONT analysis ([21]) reveals the presence of a cusp bifurcation: two saddle-node bifurcation lines delimiting a bistable region, whose origin corresponds to the cusp point (see Figure 13a). Within this region, the system exhibits bistability, whereas outside it the dynamics is

monostable. The upper region outside the bistable region is associated to high levels of $NF\text{-}\kappa B$ corresponding to TNBC subtype, while the lower region corresponds to HER2+.

It is worth noting that the bistable region in the cusp bifurcation diagram is an unbounded set. In particular, for any fixed $k_3 > 0$, the bifurcation diagram with respect to k_{12}, Figure 13b, exhibits the characteristic S-shaped curve, a typical signature of saddle-node bifurcations in bistable systems.

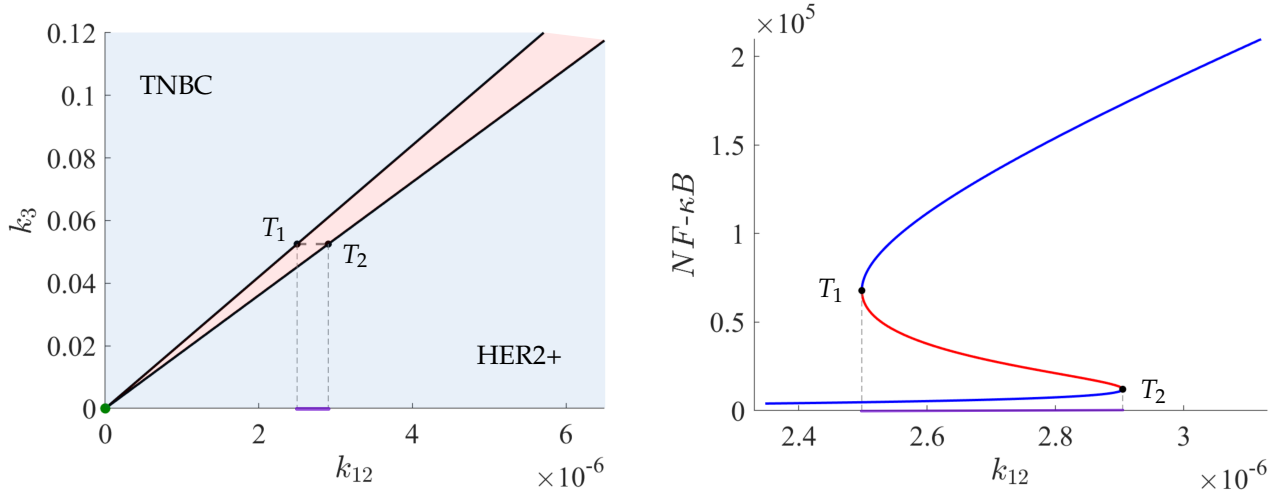

(A) $k_{12} \times k_3$ (B) $k_{12} \times NF\text{-}\kappa B$

FIGURE 13. (A) Cusp bifurcation diagram with respect to k_3 and k_{12}. The green dot indicates the cusp point, the red region represents bistability, and the blue region represents monostability. The purple line corresponds to the limits of the bistable region for a given value of k_3. (B) Bifurcation diagram with respect to k_{12} for $k_3 = 0.05250597525$. The purple line corresponds to the same interval shown in (A).

To determine the concentrations of $NF\text{-}\kappa B$ associated with the values of k_3 and k_{12} that define the two lines of the cusp bifurcation diagram (Figure 13a), we constructed a 3D plot with an additional axis representing $NF\text{-}\kappa B$ (Figure 14a). Along each line of the cusp bifurcation diagram, the combined variation of k_3 and k_{12} keeps the levels of $NF\text{-}\kappa B$ associated with each line unchanged. This behavior arises from the role of $p65$ in the reactions associated with k_3 and k_{12}. Although an increase in k_3 reduces $p65$ levels through the reaction $p65 \to 0$, and consequently decreases the availability of reactants in the reaction $p50 + p65 \to NF\kappa B$, this effect is compensated by the simultaneous increase in k_{12}. These compensatory effects result in preserved levels of $NF\text{-}\kappa B$.

Interestingly, for $p65$ levels, the combined variation of k_3 and k_{12} along both lines of the cusp diagram produces a reinforcing rather than compensatory effect. Since both reactions associated with k_3 and k_{12} reduce $p65$ levels, changing both parameters simultaneously results in a strong nonlinear reduction in $p65$ concentrations (Figure 14b).

Building on the observations regarding $NF\text{-}\kappa B$ and $p65$, the behavior of the remaining variables along the bifurcation lines can be understood from the stationary conditions of the GRN (1). Specifically, the concentrations of $N0p50$, $RNAp50$, $N0p65$, and $RNAp65$ remain constant, as each of these variables depends either on $NF\text{-}\kappa B$ or on other invariants along the lines (Figure S17). For example, the stationary condition for $N0p50$ is

$$k_5(-N0p50 + 2) - k_6 NF\text{-}\kappa B\, N0p50 = 0.$$

Since k_5 and k_6 are constants and $NF\text{-}\kappa B$ does not vary along the lines, $N0p50$ remains invariant. Similarly, for $RNAp50$ we have

$$k_{15} - k_2 RNAp50 + k_7(-N0p50 + 2) = 0,$$

which implies that $RNAp50$ is also constant, as $N0p50$ does not change. The same reasoning applies to $N0p65$ and $RNAp65$, which are directly linked to these invariants. For $p50$, the stationary condition reads

$$-k_1 p50 + k_{11} NF\text{-}\kappa B - k_{12} p50\, p65 + k_{13} RNAp50 = 0.$$

Here, $p50$ depends explicitly on both $NF\text{-}\kappa B$ and $p65$, as well as $RNAp50$. Along the bifurcation lines, $NF\text{-}\kappa B$ and $RNAp50$ remain constant. Increasing k_3 reduces the levels of $p65$, through the association reaction $p50 + p65 \to NF\text{-}\kappa B$, this reduction in $p65$ would tend to decrease $NF\kappa B$ and, consequently, lower $p50$. However, a concurrent

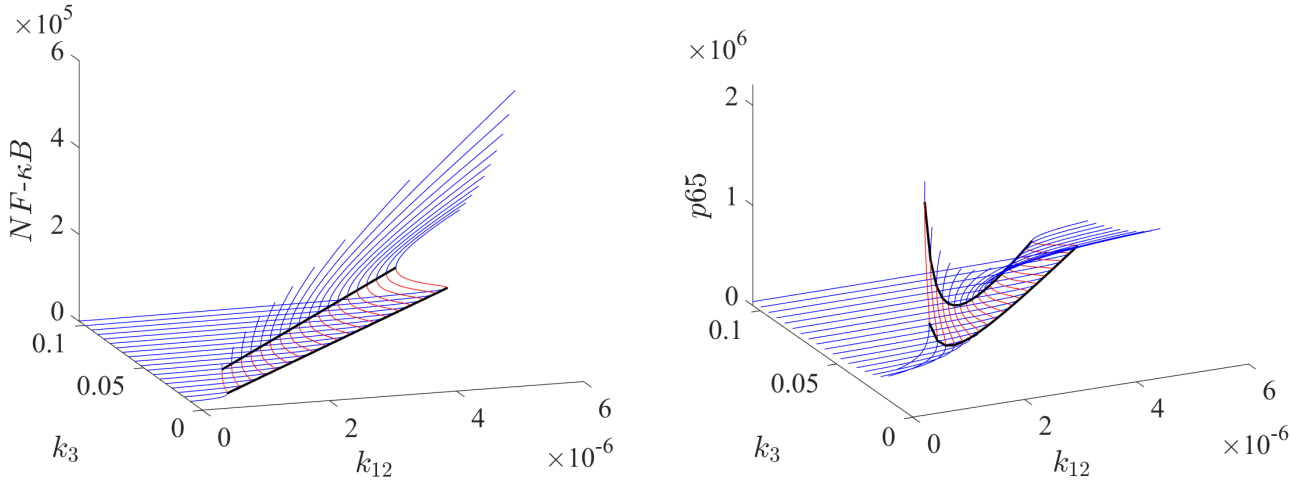

(A) $k_3 \times k_{12} \times NF\text{-}\kappa B$ (B) $k_3 \times k_{12} \times p65$

FIGURE 14. Three-dimensional bifurcation diagrams with free parameters k_3 and k_{12}. Subfigure (A) shows the behavior of $NF\text{-}\kappa B$, while subfigure (B) depicts the behavior of $p65$.

increase in k_{12} compensates for the drop in $p65$ by sustaining $NF\text{-}\kappa B$ levels. Under these conditions, the stationary balance above ensures that $p50$ remains effectively invariant despite the reduction in $p65$.

Since the levels of the $NF\text{-}\kappa B$ subunits, $p65$ and $p50$, strongly depends on its corresponding RNAs, we next turn our attention to the parameters k_7 and k_{10}, which correspond to the synthesis of $RNAp50$ ($N1p50 \rightarrow N1p50 + RNAp50$) and $RNAp65$ ($N1p65 \rightarrow N1p65 + RNAp65$), respectively. In this case, the bifurcation diagram exhibits two cusp points, $(8.0877, 168.6359)$ and $(86.8949, 16.8721)$, connected by two saddle-node bifurcation curves (Figure 15a). The bistable region delimited by these curves is a bounded set. Outside this region the system exhibits monostable behavior. Differently from the previous case, there are some intervals ($k_7 < 16.8721$, $k_7 > 86.8949$, $k_{10} < 8.0877$ and $k_{10} > 168.6359$) where a frontier between the HER2+ and TNBC regions is not well defined. To better characterize the subtypes associated to these regions, we built a 3D plot including the $NF\text{-}\kappa B$ axis, Figure 15b, which shows that within the closed region, the bifurcation diagram exhibits an S-shaped curve, reflecting the bistable behavior.

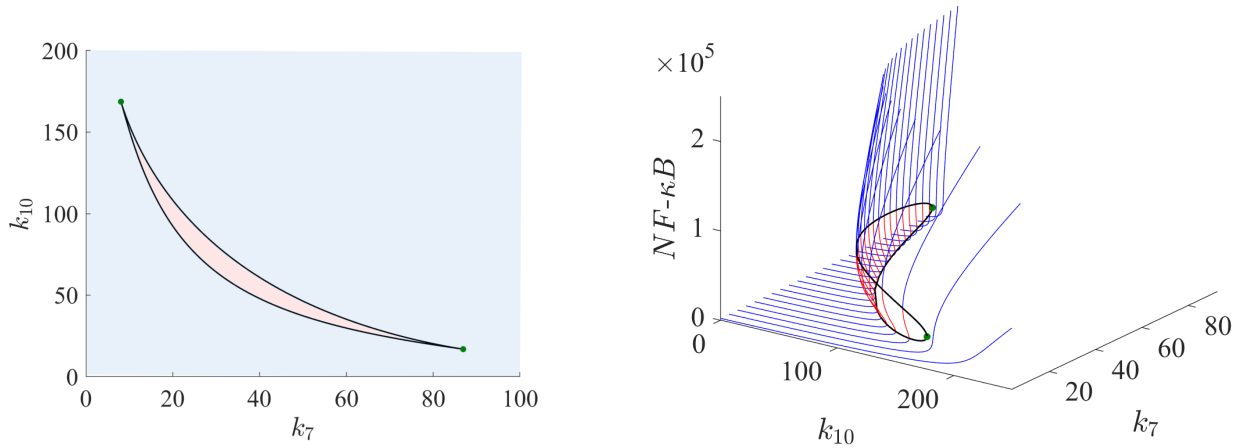

(A) $k_7 \times k_{10}$ (B) $k_7 \times k_{10} \times NF\text{-}\kappa B$

FIGURE 15. Bifurcation diagrams with free parameters k_7 and k_{10}. Subfigure (A) shows the bifurcation diagram in the parameter space: the green dots correspond to cusp points, the red region represents bistability, and the blue region represents monostability. Subfigure (B) presents the three-dimensional bifurcation diagram including the variable $NF\text{-}\kappa B$.

To better visualize the differences between each region in Figure 15b, we plot three representative $NF\text{-}\kappa B$ level curves for different values of k_7 in Figure 16. For $k_7 < 8.0877$, as shown in Figure 16a, $NF\text{-}\kappa B$ increases continuously with k_{10}. For the chosen value $k_7 = 3.706962815$, when $k_{10} \lesssim 200$, $NF\text{-}\kappa B$ levels are compatible with the HER2+ subtype, whereas for higher k_{10} values, they progressively increase toward TNBC-compatible levels.

For k_7 within the interval $(8.0877, 86.8949)$ the bifurcation diagram with respect to k_{10} (Figure 16b) exhibits an S-shaped curve, indicating bistability. For $k_7 > 86.8949$, $NF\text{-}\kappa B$ increases continuously with k_{10}. In the specific case $k_7 = 92.67407038$, $NF\text{-}\kappa B$ levels correspond to the HER2+ subtype when $k_{10} \lesssim 15$, shifting toward TNBC-like levels as k_{10} increases (Figure 16c).

It is worth highlighting that the HER2+ to TNBC transition within the bistable region occurs under fixed parameter values, as the result of stochastic variations in the proteins and RNAs levels (see [17]). Consequently, outside this region, where only one stationary point exists, a HER2+ cell cannot expontaneously progress to the TNBC subtype, since no significative variation in parameter values are expected. However, under special conditions like mutations, the HER2+ to TNBC transition could happen, even outside the bistable regions.

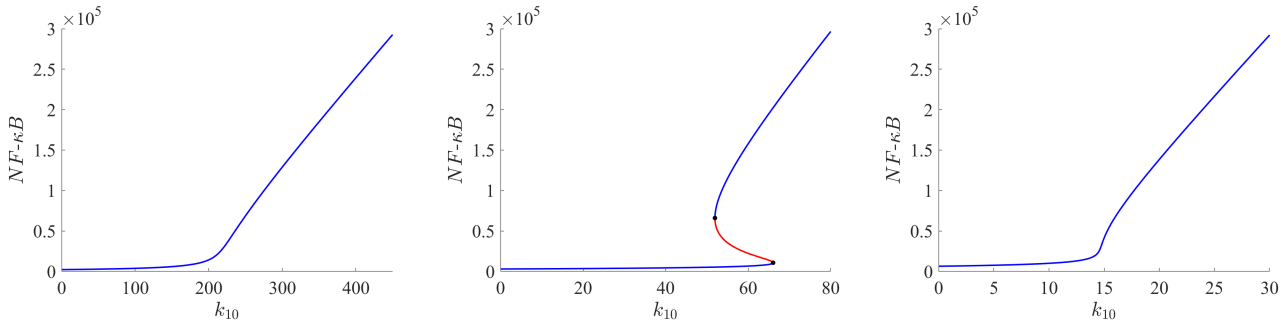

(A) $k_7 = 3.706962815$ (B) $k_7 = 37.06962815$ (C) $k_7 = 92.67407038$

FIGURE 16. Bifurcation diagrams with only k_{10} free for different values of k_7.

This study reveals that the geometry of the bistable region is strongly parameter-dependent. For k_3 and k_{12}, the region is unbounded, with a single cusp point, whereas for k_7 and k_{10} it is limited, with two cusp points. These results highlight how different parameter combinations can generate qualitatively distinct behaviors, emphasizing the system's sensitivity to parametric changes and the importance of understanding these regions to interpret potential transitions between biological states, such as HER2+ and TNBC.

3. MATERIALS AND METHODS

3.1. **Saddle-node bifurcation.** To rigorously understand the qualitative changes observed in the system dynamics as parameters vary, we first recall the mathematical conditions under which a saddle-node bifurcation occurs. Consider a smooth one-parameter family of vector fields:

$$\dot{x} = f(x, \mu), \quad x \in \mathbb{R}^n,\ \mu \in \mathbb{R},$$

and suppose that for some (x_0, μ_0), we have $f(x_0, \mu_0) = 0$, that is, x_0 is an stationary point at the parameter value μ_0. Let $A = D_x f(x_0, \mu_0)$ be the Jacobian matrix evaluated at this point.

We say that the system undergoes a saddle-node bifurcation at (x_0, μ_0) if the following conditions are satisfied:

(1) The matrix A has a simple eigenvalue equal to zero, and all other eigenvalues have nonzero real part;
(2) Let v be the right eigenvector ($Av = 0$) and w the left eigenvector ($A^\top w = 0$) associated with the zero eigenvalue. Then, the nondegeneracy and transversality conditions are, respectively,

$$w^\top \frac{\partial f}{\partial \mu}(x_0, \mu_0) \neq 0 \quad \text{and} \quad w^\top D_x^2 f(x_0, \mu_0)[v, v] \neq 0.$$

These conditions ensure the local existence of a smooth curve of equilibria tangent to the parameter axis at (x_0, μ_0). As the parameter μ crosses the bifurcation value μ_0, the system transitions from having no stationary point near x_0 to having two stationary points: one stable and one unstable (or vice versa). This behavior characterizes a saddle-node bifurcation.

Figure 17 depicts the characteristic behavior of a saddle-node bifurcation in the one-dimensional system $\dot{x} = \mu - x^2$, with $(x_0, \mu_0) = (0, 0)$ representing the saddle-node point.

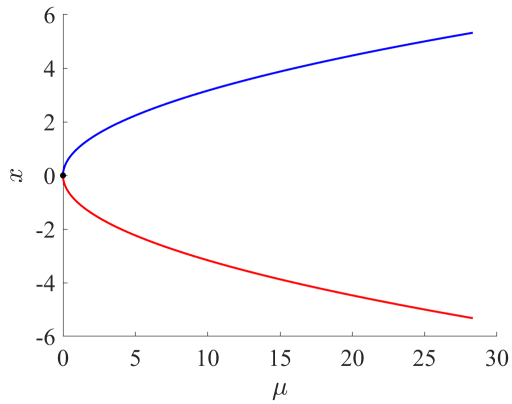

FIGURE 17. Saddle-node bifurcation diagram. The blue curve represents stable points, the red curve represents unstable points, and the black point represents the saddle-node point.

3.2. **Cusp bifurcation.** To characterize the qualitative changes in the system as two parameters vary, it is useful to recall the mathematical conditions for a cusp bifurcation. Consider a smooth two-parameter family of vector fields:

$$\dot{x} = f(x, \mu_1, \mu_2), \quad x \in \mathbb{R}^n, \ (\mu_1, \mu_2) \in \mathbb{R}^2,$$

and suppose that at some point (x_0, μ_1^0, μ_2^0), we have $f(x_0, \mu_1^0, \mu_2^0) = 0$, that is, x_0 is stationary point at the parameter values (μ_1^0, μ_2^0). Let $A = D_x f(x_0, \mu_1^0, \mu_2^0)$ be the Jacobian matrix evaluated at this point.

The system undergoes a cusp bifurcation at (x_0, μ_1^0, μ_2^0) if the following conditions hold:

(1) The Jacobian matrix A has a simple eigenvalue equal to zero, and all other eigenvalues have nonzero real part;
(2) Let v be the right eigenvector and w the left eigenvector associated with the zero eigenvalue. Then the following nondegeneracy conditions are satisfied:

$$w^\top \frac{\partial f}{\partial \mu_1}(x_0, \mu_1^0, \mu_2^0) = 0, \quad w^\top \frac{\partial f}{\partial \mu_2}(x_0, \mu_1^0, \mu_2^0) \neq 0,$$

$$w^\top D_x^2 f(x_0, \mu_1^0, \mu_2^0)[v, v] = 0, \quad w^\top D_x^3 f(x_0, \mu_1^0, \mu_2^0)[v, v, v] \neq 0.$$

Specifically, a cusp bifurcation arises when two saddle-node bifurcation points merge and annihilate each other as the parameters vary. In parameter space, this gives rise to a bifurcation curve forming a cusp, which separates regions with different numbers of equilibria.

3.3. **MATCONT.** The bifurcation analyses were performed using MATCONT (version 7.6) [21], a *MATLAB*-based package for numerical continuation and stability analysis of dynamical systems defined by ordinary differential equations. The mathematical model considered is described in Section 2, and the numerical continuation was carried out with respect to different parameters of the model.

In the `Continuer` tab of MATCONT, the following settings were adopted for the bifurcation analyses:

- `InitStepsize` = 100
- `MinStepsize` = 100
- `MaxStepsize` = 1000
- `MaxNewtonIters` = 3
- `MaxCorrIters` = 10
- `MaxTestIters` = 10
- `VarTolerance` = 10^{-6}
- `FunTolerance` = 10^{-6}
- `TestTolerance` = 10^{-5}
- `Adapt` = 3
- `MaxNumPoints` = varied depending on the case
- `CheckClosed` = 50
- `Jacobian Increment` = 10^{-5}

All computations were carried out in *MATLAB* R2024a (Update 7) running on Windows 11, with MATCONT version 7.6.

3.4. **COPASI.** Stochastic simulations were performed using *COPASI* (version 4.45) [22], a software tool for modeling and simulation of biochemical networks. The simulations employed the τ-Leap stochastic algorithm with the following settings: $\varepsilon = 0.001$, maximum number of internal steps $= 1.215752192 \times 10^7$, and a random seed fixed to 1.

Each simulation was run for an initial period of 262,800 minutes (approximately 6 months), with outputs recorded every 1 minute. If no transition occurred within this period, the simulation was extended iteratively in additional 6-month intervals until the transition was observed. If the transition did not occur within 20 years of simulated time, the run was terminated. Initial conditions were set at the steady state of the deterministic model whenever required.

4. DISCUSSION

A central question in the study of transitions between stable states in nonlinear dynamical systems is which dynamical features effectively control transition probabilities. In many theoretical frameworks, this control is often interpreted in terms of potential depth. However, in non-conservative systems, such as gene regulatory networks, potential functions are generally non-unique and do not uniquely determine the system's dynamics, which limits their explanatory and predictive power.

Our results provide an alternative and more general perspective by showing that the phase-space distance between stationary states is a critical determinant of transition probabilities. Unlike potential-based measures, state-space distances are well defined in non-equilibrium systems and can, in principle, be estimated experimentally. In this context, the bifurcation structure of the system plays a key role in shaping how such distances emerge and constrain accessible transitions between stable states.

Importantly, the mere coexistence of multiple stable states is only a necessary, but not sufficient, condition for transitions to occur. The presence of two basins of attraction does not, by itself, imply that transitions between them are likely or even dynamically accessible on relevant timescales. Instead, transition probabilities are shaped by how these basins are arranged in phase space and, in particular, by the distance separating stable states from the intervening unstable states. From this perspective, phase-space distance acts as an effective control parameter, simultaneously constraining the likelihood, timescale, and variability of transitions. This form of control is inherently geometric rather than energetic, and does not rely on the existence of a well-defined potential function.

In addition to the role of phase-space distance, our previous analysis of the NF-κB regulatory system [17] demonstrated that the local dynamical structure of the intervening unstable stationary state further constrains transition dynamics. Linear stability analysis revealed that this state possesses a single unstable eigendirection associated with a small positive eigenvalue, while all remaining directions are strongly contracting. This configuration generates a narrow one-dimensional escape channel embedded within a predominantly attracting local flow. Stochastic trajectories approaching this region are therefore funneled toward the unstable manifold, and once the vicinity of the saddle is reached, crossing occurs rapidly along this weakly unstable direction. In this sense, the unstable state functions as a geometric gateway between basins: the dominant constraint lies in reaching its neighborhood, whereas escape beyond it is dynamically swift. This mechanism reinforces the geometric character of transition control in non-conservative systems, where the local eigenspectrum and the global phase-space distances jointly determine accessibility, irreversibility, and variability of phenotypic transitions.

Within this geometric framework, our bifurcation analysis reveals a marked asymmetry in the sensitivity of the two stable states to parameter variations. Across all model parameters, the HER2+ branch consistently exhibits low sensitivity, with NF-κB levels remaining relatively invariant even under substantial parameter changes. This behavior suggests that, in this regime, NF-κB effectively buffers intrinsic parameter variability in upstream processes, acting as a dynamical filter that suppresses the transmission of such variability across the network.

In contrast, the TNBC branch displays pronounced sensitivity to the same parameter variations, with small parameter changes leading to large variations in NF-κB levels. In this regime, intrinsic parameter variability is not attenuated but instead amplified by the network architecture, resulting in heightened variability of the system's state. This intrinsic dynamical instability provides a natural interpretation for the extensive intra- and intertumoral variability observed in TNBC, as well as for the large number of molecular subclassifications proposed for this subtype [5, 6]. From this perspective, the clinical variability associated with TNBC emerges as a direct consequence of its underlying dynamical organization, rather than solely from genetic or environmental differences.

Beyond sensitivity at fixed parameter values, our two-parameter bifurcation analysis shows that the global geometry of the bistable region itself depends critically on the choice of regulatory mechanisms being perturbed. In particular, different parameter combinations give rise to qualitatively distinct cusp geometries, resulting in

either unbounded or limited bistable regions in parameter space. Unbounded regions imply that bistability can persist over wide ranges of parameter variation, allowing stable states to remain dynamically accessible despite substantial intrinsic variation. In contrast, bounded bistable regions impose strict limits on the parameter ranges compatible with multistability, beyond which one of the stable states disappears altogether.

From a dynamical perspective, these geometric differences introduce an additional level of constraint on phenotypic transitions. While phase-space distance governs transition probabilities within a bistable regime, the cusp geometry determines whether such a regime exists at all under parameter variation. As a result, the accessibility of transitions is controlled not only by distances between states, but also by the global structure of the bifurcation set that organizes the emergence and destruction of attractor basins. This highlights the role of cusp bifurcations as higher-order organizing centers that delimit the regions of phenotypic plasticity in non-conservative regulatory networks.

Taken together, our results establish a geometric framework in which transitions in non-conservative regulatory networks are controlled by a hierarchy of structural features, including phase-space distances between stable states, their sensitivity to intrinsic parameter perturbations, and the global organization imposed by cusp bifurcations. Importantly, this framework does not rely on system-specific molecular details and is therefore expected to apply broadly to gene regulatory networks and other nonlinear dynamical systems operating far from equilibrium.

The present analysis focuses on how distances and bifurcation geometry constrain transition probabilities and times under parameter variation. An additional dynamical aspect that remains outside the scope of this work concerns the observation that identical phase-space distances between stationary states do not necessarily produce identical transition-time distributions. As evidenced by the transition-time statistics reported here, different kinetic perturbations that yield the same separation between states can still lead to distinct stochastic escape dynamics. This indicates that, beyond distance, further structural properties of the underlying flow influence transition statistics. Characterizing these additional geometric–dynamical factors represents a natural extension of the present framework and will be addressed in subsequent work.

Acknowledgments

The authors acknowledge the Laboratório Nacional de Computação Científica (LNCC/MCTI, Brazil) for providing access to the Santos Dumont supercomputer and a MATLAB license. The authors also thank the High Performance Computer Center (NACAD) - COPPE/Federal University of Rio de Janeiro (UFRJ), which has supported this research. Website: http://nacad.ufrj.br.

Funding: Mayara Caldas was supported by Coordenação de Aperfeiçoamento de Pessoal de Nível Superior - Brasil (CAPES), grant number 88887.946674/2024-00.

References

[1] Hyuna Sung, Jacques Ferlay, Rebecca L Siegel, Mathieu Laversanne, Isabelle Soerjomataram, Ahmedin Jemal, and Freddie Bray. Global cancer statistics 2020: Globocan estimates of incidence and mortality worldwide for 36 cancers in 185 countries. *CA: a cancer journal for clinicians*, 71(3):209–249, 2021.

[2] Fabiana Lüönd, Stefanie Tiede, and Gerhard Christofori. Breast cancer as an example of tumour heterogeneity and tumour cell plasticity during malignant progression. *British journal of cancer*, 125(2):164–175, 2021.

[3] Patrick Maisonneuve, Davide Disalvatore, Nicole Rotmensz, Giuseppe Curigliano, Marco Colleoni, Silvia Dellapasqua, Giancarlo Pruneri, Mauro G Mastropasqua, Alberto Luini, Fabio Bassi, et al. Proposed new clinicopathological surrogate definitions of luminal a and luminal b (her2-negative) intrinsic breast cancer subtypes. *Breast Cancer Research*, 16(3):R65, 2014.

[4] Xin Xiong, Le-Wei Zheng, Yu Ding, Yu-Fei Chen, Yu-Wen Cai, Lei-Ping Wang, Liang Huang, Cui-Cui Liu, Zhi-Ming Shao, and Ke-Da Yu. Breast cancer: pathogenesis and treatments. *Signal transduction and targeted therapy*, 10(1):49, 2025.

[5] Brian D Lehmann, Bojana Jovanović, XI Chen, Monica V Estrada, Kimberly N Johnson, Yu Shyr, Harold L Moses, Melinda E Sanders, and Jennifer A Pietenpol. Refinement of triple-negative breast cancer molecular subtypes: implications for neoadjuvant chemotherapy selection. *PloS one*, 11(6):e0157368, 2016.

[6] Matthew D Burstein, Anna Tsimelzon, Graham M Poage, Kyle R Covington, Alejandro Contreras, Suzanne AW Fuqua, Michelle I Savage, C Kent Osborne, Susan G Hilsenbeck, Jenny C Chang, et al. Comprehensive genomic analysis identifies novel subtypes and targets of triple-negative breast cancer. *Clinical Cancer Research*, 21(7):1688–1698, 2015.

[7] Eluri Pavitra, Jyothsna Kancharla, Vivek Kumar Gupta, Kiran Prasad, Ju Yong Sung, Jigyeong Kim, Mandava Bhuvan Tej, Rino Choi, Jeong-Hwan Lee, Young-Kyu Han, et al. The role of nf-κb in breast cancer initiation, growth, metastasis, and resistance to chemotherapy. *Biomedicine & pharmacotherapy*, 163:114822, 2023.

[8] Wei Wang, Subhasree A Nag, and Ruiwen Zhang. Targeting the nfκb signaling pathways for breast cancer prevention and therapy. *Current medicinal chemistry*, 22(2):264–289, 2015.

[9] Woosung Chung, Hye Hyeon Eum, Hae-Ock Lee, Kyung-Min Lee, Han-Byoel Lee, Kyu-Tae Kim, Han Suk Ryu, Sangmin Kim, Jeong Eon Lee, Yeon Hee Park, et al. Single-cell rna-seq enables comprehensive tumour and immune cell profiling in primary breast cancer. *Nature communications*, 8(1):15081, 2017.

[10] Sunny Z Wu, Ghamdan Al-Eryani, Daniel Lee Roden, Simon Junankar, Kate Harvey, Alma Andersson, Aatish Thennavan, Chenfei Wang, James R Torpy, Nenad Bartonicek, et al. A single-cell and spatially resolved atlas of human breast cancers. *Nature genetics*, 53(9):1334–1347, 2021.

[11] CH Waddington. The strategy of the genes. allen, 1957.
[12] Stuart Kauffman. Differentiation of malignant to benign cells. *Journal of theoretical biology*, 31(3):429–451, 1971.
[13] Sui Huang, Ingemar Ernberg, and Stuart Kauffman. Cancer attractors: a systems view of tumors from a gene network dynamics and developmental perspective. *Seminars in Cell & Developmental Biology*, 20(7):869–876, 2009.
[14] Bruno RB Pires, Andre L Mencalha, Gerson M Ferreira, Waldemir F De Souza, José A Morgado-Díaz, Amanda M Maia, Stephany Corrêa, and Eliana SFW Abdelhay. Nf-kappab is involved in the regulation of emt genes in breast cancer cells. *PloS one*, 12(1):e0169622, 2017.
[15] Myong-Hee Sung, Ning Li, Qizong Lao, Rachel A Gottschalk, Gordon L Hager, and Iain DC Fraser. Switching of the relative dominance between feedback mechanisms in lipopolysaccharide-induced nf-κb signaling. *Science signaling*, 7(308):ra6–ra6, 2014.
[16] Heike L Pahl. Activators and target genes of rel/nf-κb transcription factors. *Oncogene*, 18(49):6853–6866, 1999.
[17] Francisco Lopes, Bruno RB Pires, Alexandre AB Lima, Renata Binato, and Eliana Abdelhay. Nf-κb epigenetic attractor landscape drives breast cancer heterogeneity. *npj Systems Biology and Applications*, 11(1):135, 2025.
[18] Francisco JP Lopes, Fernando MC Vieira, David M Holloway, Paulo M Bisch, and Alexander V Spirov. Spatial bistability generates hunchback expression sharpness in the drosophila embryo. *PLoS computational biology*, 4(9):e1000184, 2008.
[19] Chieh Hsu, Vincent Jaquet, Mumun Gencoglu, and Attila Becskei. Protein dimerization generates bistability in positive feedback loops. *Cell reports*, 16(5):1204–1210, 2016.
[20] James H. Espenson. *Chemical Kinetics and Reaction Mechanisms*. McGraw-Hill, 1995.
[21] A. Dhooge and W. Govaerts and Yu.A. Kuznetsov and H.G.E. Meijer and B. Sautois. Matcont: A MATLAB package for numerical bifurcation analysis of ODEs, 2003–2023. Disponível em: `http://www.matcont.ugent.be/`.
[22] Stefan Hoops, Sven Sahle, Rainer Gauges, Christian Lee, Jürgen Pahle, Nils Simus, Manish Singhal, Lijun Xu, Pedro Mendes, and Ursula Kummer. Copasi: a complex pathway simulator. *Bioinformatics*, 22(24):3067–3074, 2006.